This is a “preproof” accepted article for *Mineralogical Magazine*.
This version may be subject to change during the production process.
10.1180/mgm.2024.87

Crystal chemistry and Raman spectroscopy of the johnbaumite - hydroxylellestadite mineral series and associated As- and B-bearing minerals from pyrometamorphic xenolith of the Upper Chegem Caldera, North Caucasus, Kabardino-Balkaria, Russia.

Dorota Środek[1*], Mateusz Dulski[2], Katarzyna Balin[3]

[1]University of Silesia, Faculty of Natural Sciences, Institute of Earth Science, Będzińska 60, Sosnowiec, Poland

[2]University of Silesia, Institute of Materials Engineering, Silesian Center for Education and Interdisciplinary Research, 75 Pułku Piechoty 1A, 41-500 Chorzów, Poland

[3]A. Chełkowski Institute of Physics, University of Silesia, 75 Pułku Piechoty 1A, 41-500 Chorzów, Poland

*corresponding author: dorota.srodek@us.edu.pl

Abstract

A calcium-silicate xenolith (no. 11) from the ignimbrite of the Upper Chegem Caldera in Kabardino-Balkaria, Russia, reveals a diverse mineral assemblage with As- and B-bearing phases from the apatite supergroup such as svabite and johnbaumite-hydroxylellestadite series, in additon to cahnite and datolite. Three distinct zones of variable arsenic content have been investigated. Notably, the outermost altered zone adjacent to the ignimbrite hosts the highest concentration of arsenic and arsenate minerals. A detailed structural analysis using Raman spectroscopy was carried out to investigate the distribution of boron and arsenic in tetrahedral coordination. This provides the basis for describing a solid-solution system between hydroxylellestadite, svabite, and johnbaumite as a novel for the apatite supergroup minerals. The analysis was aimed to elucidate the origin of varying element contents, particularly in relation to the distance from the xenolith-ignimbrite contact. The presence of boron and arsenic, probably derived from ignimbrites, highlights the important role of volcanic rocks as potential contributors of these elements in mineral formation processes.

Keywords: johnbaumite, hydroxylellestadite, svabite, pyrometamorphic rocks, cahnite, boron, arsenic minerals, apatite supergroup, Raman spectroscopy

Introduction

The xenoliths of the Upper Chegem Caldera ignimbrites are fascinating objects for modern mineralogy. They combine altered rocks of different lithologies, such as

schist, granite, sandstone, siltstone, argillite, and limestone (Bogatikov et al., 1992). Most notable are the large carbonate-silicate xenoliths up to 20 m in diameter formed as a result of pyrometamorphism. There are 11 known xenoliths of this type in the area (Galuskina et al., 2015). The xenoliths represent rare high-temperature and low-pressure mineral associations containing new and rare minerals formed under sanidinite facies . The most recent xenolith (no. 11) was found in 2012, and to date, there is minimal information on its mineralogy (Galuskina et al., 2015).

The examination of xenolith no. 11 revealed the presence of calcium-arsenate members of the apatite supergroup - svabite, $Ca_5(AsO_4)_3F$, johnbaumite, $Ca_5(AsO_4)_3(OH)$, and As-bearing hydroxylellestadite, which were found together with previously unobserved cahnite, $Ca_2[B(OH)_4](AsO_4)$, and datolite, $CaB(SiO_4)(OH)$. As-bearing minerals have been reported from other previously discovered xenoliths of the Upper Chegem Caldera. Svabite, As-bearing apatite, and As-bearing hydroxylellestadite were described by Banasik et al. (2012). In addition, the chemical composition and single-crystal X-ray data of B- and As-bearing galuskinite, $Ca_7(SiO_4)_3CO_3$, were obtained by Lazic et al. (2012).

Svabite is a member of the apatite group (the apatite supergroup) (Pasero et al., 2010). The general chemical formula of this supergroup is presented as $^{IX}M1_2{}^{VII}M2_3(^{IV}TO_4)_3X$, and in the ideal svabite $M1$=$M2$=Ca, T=As, and X=F (Biagioni et al., 2016). In the studied rock, svabite was confirmed only in the outer part of the xenolith. In other xenolith zones, OH groups substituted mainly F at the *X* site. Then, we were able to distinguish another member of the arsenate apatite group member – johnbaumite, $Ca_5(AsO_4)_3OH$ (Biagioni & Pasero, 2013). In some cases, we also observed a substitution of As by Si and S at the *T* site. Therefore, the third mineral of the apatite supergroup – hydroxylellestadite, $Ca_5(SiO_4)_{1.5}(SO_4)_{1.5}OH$, was

distinguished in this xenolith. All three of the above mentioned members of the apatite supergroup crystallize in the $P6_3/m$ space group (Onac et al., 2006; Biagioni & Pasero, 2013; Biagioni et al., 2016). They are also topologically similar - their structure consists of columns of face-sharing *M*1 polyhedra running along **c**. These polyhedra are typically referred to as metaprisms (Pasero et al., 2010), and are connected by TO_4 tetrahedra with channels containing *M*2 cations and X anions (Onac et al., 2006; Biagioni & Pasero, 2013; Biagioni et al., 2016).

Svabite is associated with boron-rich minerals such as cahnite and datolite in the outer zone of the xenolith no. 11. Cahnite, a relatively rare mineral in nature, has a structure comparable to that of zircon, with $(AsO_4)^{3-}$ and $[B(OH)_4]^{1-}$ tetrahedra alternately occuping the Si site, and CaO_8 polyhedra between them instead of ZrO_8 (Prewitt & Buerger, 1961). Low-temperature spheroidal mineral aggregates also occur in this zone. These are noteworthy because they consist mainly of fine-crystalline bultfonteinite, which contains arsenic in its structure (about 3.67 - 6.40 wt.% As_2O_5), calcite, and fluorite. A similar low-temperature association was previously described from xenolith no. 1 in the Upper Chegem Caldera (Zadov et al., 2013).

This work provides spectroscopic data on the chemical composition of apatite supergroup minerals and associated As- and B-bearing phases from xenolith no. 11 of the Upper Chegem Caldera. This study is a part of the current trend of using Raman data to distinguish between individual group members and supergroups of minerals (Leissner et al., 2015; Watenphul et al., 2016; Bersani et al., 2019; Varlamov et al., 2020). We focused mainly on the Raman scattering arising from vibrations associated with TO_4 tetrahedra, as concentration on modes related to the sites within the structural channels would not yield the expected results since the bands associated

with vibrations of the OH group showed very low intensity (Supplementary materials, Fig. S1).

Experimental methods

The chemical composition and crystal morphology of the minerals studied were investigated using a Phenom XL analytical scanning electron microscope (Faculty of Natural Sciences, University of Silesia, Poland). More detailed chemical analyses were carried out using a CAMECA SX100 electron microprobe (Institute of Geochemistry, Mineralogy, and Petrology, University of Warsaw, Poland). EDS-WDS chemical maps were also made using the electron microprobe analyzer. The following lines and standards were used: Ca*K*α, Si*K*α - diopside; S*K*α - barite; P*K*α, F*K*α - apatite BB2; V*K*α - V_2O_5; As*L*α - GaAs; Cl*K*α - tugtupite. The accelerating voltage was 15 kV, and the beam diameter was 10 μm.

Infrared reflectance spectra were measured using a Bio-Rad FTS-6000 spectrometer equipped with a Bio-Rad UMA-500 microscope with a mercury cadmium telluride (MTC) detector cooled to 77 K with liquid nitrogen. Spectra were obtained in the 6000–700 cm^{-1} range with a resolution of 4 cm^{-1}. A spectrum of a gold-covered reference slide was collected as a background, and the spectrum of the sample was recorded by accumulating 1248 scans. The reflectance data were converted to standard absorption spectra using Kramers-Krönig transformations. Measurements were performed on *in-situ* grains.

Raman measurements were carried out using a WITec CRM alpha 300R confocal Raman microscope equipped with an air-cooled solid-state laser (λ=532 nm) and a CCD camera. The excitation laser radiation was delivered to the microscope via

polarization-maintaining single-mode optical fiber (50 μm in diameter). Data were acquired using an Olympus MPLAN 100x/0.9NA air objective. The Raman scattered light was focused onto a multimode fiber (50 μm in diameter) and monochromator with a 600 line/mm grating. The Raman signal was verified using a silicon sample by checking the Si position (520.7 cm^{-1}). All individual Raman spectra were collected in the 200-4000 cm^{-1} range with a spectral resolution of 3 cm^{-1}.

The surface Raman imaging was performed in an area 140 μm x 110 μm using 280 x 220 pixels (=61 600 spectra) with an integration time of 33 ms per spectrum and a sample movement accuracy of ±0.5 μm . All spectra were collected in the 150–4000 cm^{-1} range at 10 mW on the sample and 3 cm^{-1} spectral resolution. The output data was manipulated by performing a baseline correction using the 3rd-degree auto-polynomial function and subjected to an automatic cosmic ray removal procedure. A sum filter was first used to produce chemical images, while a K-means cluster analysis (Manhattan distance) was performed using WITec ProjectFive Plus Software (version 5.3, WITec Wissenschaftliche Instrumente und Technologie GmbH, Ulm, Germany) to show the area of occurrence of each phase. Finally, a band fitting analysis using a Lorentz–Gauss function with the minimum number of components was performed on the averaged spectrum originating from the individual sample using the GRAMS software package (version 9.2, Thermo Fisher Scientific, Waltham, MA, USA) .

Chemical analysis to detect and image boron in the investigated phases was performed using time-of-flight secondary ion mass spectrometry (TOF–SIMS). TOF-SIMS studies are complementary to EDX studies in that they can detect all elements within the detection limits in the ppm range (Hagenhoff, 2000; Fearn, 2015; Siljeström et al., 2017). A TOF-SIMS 5 mass spectrometer equipped with a reflectron-

type analyzer and a liquid metal ion gun (Bi_3^+, 30 keV, ~0.3 pA) was used to analyze two regions containing the mineral. The area analyzed was adapted to the size of the mineral grain in the material examined and was approximately 320 µm × 320 µm and 270 µm × 270 µm, respectively. The surface of the sample areas was cleaned in the spectrometer with a cesium gun immediately prior to measurements. Positive mass spectra were collected using the Spectroscopy and Fast Imaging Modes of operation. The spectra were calibrated using CH_3^+, $C_2H_3^+$, $C_3H_3^+$, and $C_3H_5^+$ ions were used for positive polarity. The SurfaceLab6 software was used for data analysis. Distribution maps were reconstructed from the mass spectra in post-measurement analysis.

Geological setting

The pyrometamorphic calc-silicate rocks are found between the Lakargii and Vorlan peaks in the Upper Chegem Caldera, located in the Baksan Valley in the eastern part of the Elbrus-Kyuygen volcanic region in the North Caucasus, Kabardino-Balkaria, Russia (Bogatikov et al., 1992). The detailed geological setting with maps can be found at Bogatikov et al. (1992) and Gazis (1995). To date, 11 altered calc-silicate xenoliths containing rare high-temperature and low-pressure mineral assemblages have been found within the ignimbrites (Galuskina et al., 2015). Among them, more than 20 new minerals have been described in recent years (Galuskin et al., 2015). The studied samples were collected in 2016 from different parts of xenolith no. 11 (Fig. 1).

Fig. 1. (A) xenolith no. 11 is distinguished by its light colour in contrast to the dark ignimbrite of the Upper Chegem Caldera; (B) contact of the xenolith with the ignimbrite, where B- and As-bearing minerals have been found; (C) the larnite zone (zone II) is the more developed zone in the xenolith containing green-yellow rondorfite crystals.

This is a recently discovered calcium-silicate xenolith with a diameter of about 5 m. It contains 3 zones characterised by different mineral compositions (Fig. 2). The

first identified as a xenolith core (zone I) contains periclase (MgO), brucite $(MgOH)_2$, As-bearing hydroxylellestadite, rondorfite ($Ca_8Mg(SiO_4)_4Cl_2$), killalaite $Ca_{6.4}(H_{0.6}Si_2O_7)_2(OH)_2$, and Ca-Mg hydrosilicates. It is a cryptocrystalline massive rock showing no lustre with colors ranging from light to dark gray. The middle zone (II) have more coarse-grained crystalline texture with single crystals visible within the grayish rock mass. It consists of larnite (Ca_2SiO_4), rustumite ($Ca_{10}(Si_2O_7)_2(SiO_4)(OH)_2Cl_2$), rankinite ($Ca_3Si_2O_7$), rondorfite, galuskinite ($Ca_7(SiO_4)_3(CO_3)$), As-bearing hydroxylellestadite, minerals of the edgrewite-hydroxyledgrewite series ($Ca_9(SiO_4)_4(F,OH)_2$), kermiasite-elbrusite ($Ca_3(Zr,U)_2(SiO_4)(Fe^{3+}O_4)_2$, Sn-bearing lakargiite ($Ca(Zr,Sn,Ti)O_3$), wadalite ($(Ca,Mg)_6(Al,Fe^{3+})_4((Si,Al)O_4)_3O_4Cl_3$), cuspidine ($Ca_8(Si_2O_7)_2F_4$) and secondary minerals: killalaite, hydrogrossular, thaumasite ($Ca_3(SO_4)[Si(OH)_6](CO_3)\cdot 12H_2O$), foshagite ($Ca_4(Si_3O_9)(OH)_2$), defernite ($Ca_6(CO_3)_{1.58}(Si2O_7)_{0.21}(OH)_7[Cl_{0.50}(OH)_{0.08}(H_2O)_{0.42}]$), and tobermorite ($Ca_4Si_6O_{17}(H_2O)_2\cdot(Ca\cdot 3H_2O)$ (Galuskina et al., 2018). The outer zone (III) is strongly altered, brittle white part of the xenolith. It consists of hydrogrossular, minerals of the thaumasite-ettringite series, fluorite (CaF_2), Ca-Al hydrosilicate, tobermorite, calcite ($CaCO_3$), svabite, cahnite and contains relics of cuspidine, perovskite ($CaTiO_3$), datolite, and lakargiite.

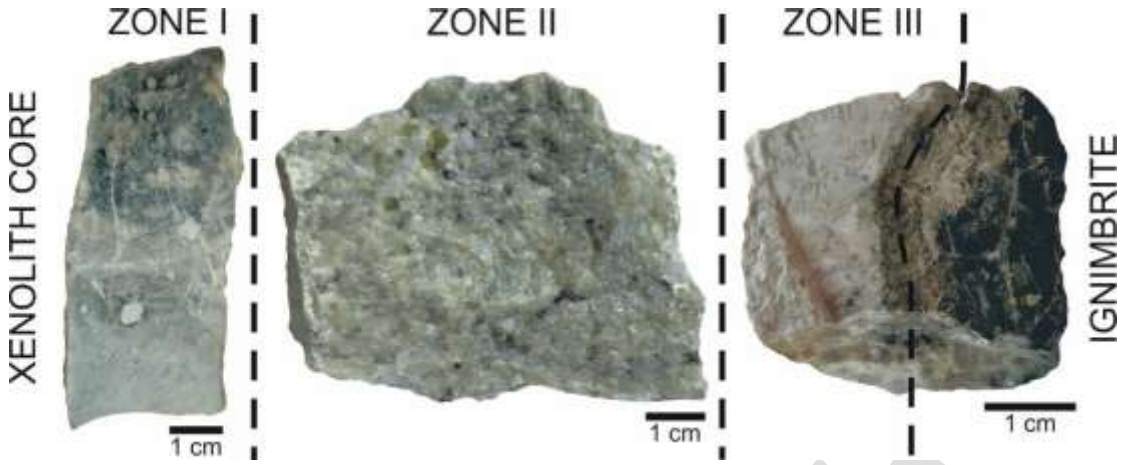

Fig. 2. Photo of representative samples of zones I, II, and III of the xenolith and its' contact with the ignimbrite.

Results

Investigation results of minerals of the apatite supergroup

Minerals belonging to the apatite supergroup within xenolith no. 11, formed irregular, elongated grains of varying sizes, reaching up to 100 micrometers. They often formed aggregates (up to 1.0 mm in diameter) of several crystals. Both the single crystals and their aggregates were usually chemically homogeneous. The only exceptions to this rule were the aggregates found in the cuspidine veins, characterized by variable chemical compositions within the *T* (As ↔ Si/S) and X (OH ↔ F) sites. Despite the homogeneity of the individual apatite supergroup minerals in the studied xenolith, their chemical composition varied throughout the xenolith zones. During the research, the following minerals of the apatite supergroup were identified in the studied rock: hydroxylellestadite (zone I, II and cuspidine veins in zone III), svabite (zone III), and johnbaumite (cuspidine veins in zone III). The results of the chemical analyses of these minerals are summarized in Table 1.

Table 1. Chemical composition of the selected apatite supergroup minerals.

	hydroxylellestadite				johnbaumite		svabite
wt%	1	2	3	4	5	6	7
SO_3	23.44	20.38	15.20	11.20	5.44	4.32	3.27
P_2O_5	0.29	0.40	7.16	8.15	11.03	10.98	9.57
V_2O_5	n.d	n.d	n.d	0.46	0.90	0.94	n.d.
SiO_2	17.58	15.28	11.43	8.39	4.16	3.26	2.41
As_2O_5	0.55	6.21	9.50	17.14	25.96	28.90	33.68
CaO	55.60	53.20	54.03	51.35	49.27	49.14	47.59
Cl	1.39	1.72	1.10	1.03	1.45	1.52	0.37
F	0.27	0.52	1.31	1.34	0.96	0.80	1.59
H_2O*	1.30	1.03	0.83	0.76	0.77	0.81	0.69
-O=F+Cl	0.43	0.61	0.80	0.80	0.73	0.71	0.75
Total	100.00	98.13	99.77	99.02	99.20	100.00	98.41
Calculated on 8 cations							
S	1.48	1.34	0.99	0.76	0.39	0.31	0.24
P	0.02	0.03	0.52	0.63	0.88	0.88	0.79
V	n.d	n.d	n.d	0.03	0.06	0.06	n.d.
Si	1.48	1.34	0.99	0.76	0.39	0.31	0.24
As	0.02	0.29	0.50	0.82	1.28	1.44	1.73
T site	**3.00**	**3.00**	**3.00**	**3.00**	**3.00**	**3.00**	**3.00**
Ca	5.00	5.00	5.00	5.00	5.00	5.00	5.00
M site	**5.00**	**5.00**	**5.00**	**5.00**	**5.00**	**5.00**	**5.00**
Cl	0.20	0.26	0.16	0.16	0.23	0.24	0.06
F	0.07	0.14	0.36	0.38	0.29	0.24	0.49
OH	0.73	0.60	0.48	0.46	0.48	0.52	0.45
X site	**1.00**	**1.00**	**1.00**	**1.00**	**1.00**	**1.00**	**1.00**

Note: * - calculated on the basis of charge balance

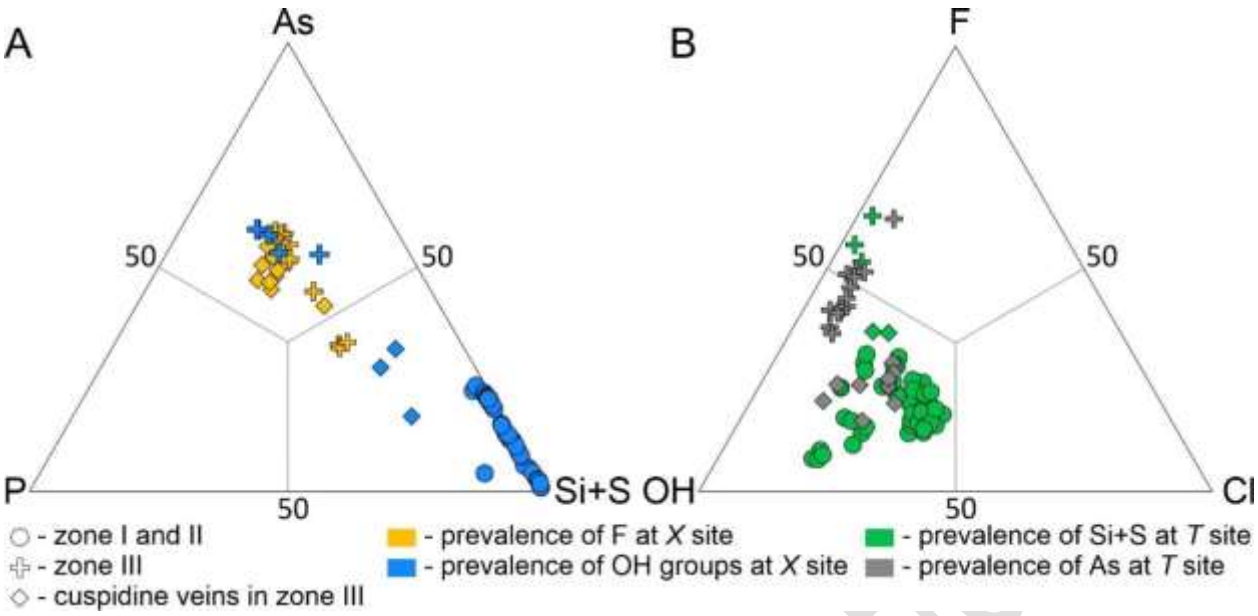

Fig. 3. Ternary diagram of (A) cations at the *T* site and (B) anions at the *X* site in the solid-solution system between hydroxylellestadite, johnbaumite and svabite. Symbols used in the diagram: circles - analyses made in the zones I and II, crosses - analyses made in the zone III, diamond - analyses made in the cuspidine veins in zone III. Colours used in the diagram: A) blue - prevalence of OH groups at *X* site, yellow - prevalence of F at *X* site, B) green - prevalence of Si+S at *T* site, grey - prevalence of As at *T* site.

In the relatively unaltered area of the xenolith (zone I), hydroxylellestadite with minor arsenic substitutions (0.55 - 6.21 wt% As_2O_5, Fig. 4A, B, Table 1.1-2,) was identified. Chemical composition analyses of apatite supergroup minerals located further from the xenolith core revealed gradual changes in the occupancy of the *T* and *X* positions within their structure (Fig. 3B). Additionally, a significant increase in arsenic content in the tetrahedral position was observed in minerals from the outermost and most altered part of the xenolith (zone II and III) (Fig. 3A). Another notable observation was the simultaneous increase in fluorine content at the expense of hydroxyl groups (Fig. 3). Consequently, in the highly weathered outer part of the xenolith, the apatite supergroup mineral was identified as svabite (zone III) (Fig. 4D;

Table 1.7). Also, cuspidine veins containing aggregates composed of apatite supergroup minerals were also noted in the outer part of the xenolith (zone III) (Fig. 4C, Fig. 5). Within these veins two members of the apatite supergroup can be distinguished - hydroxylellestadite (Table 1, 3-4) and johnbaumite (Table 1, 5-6).

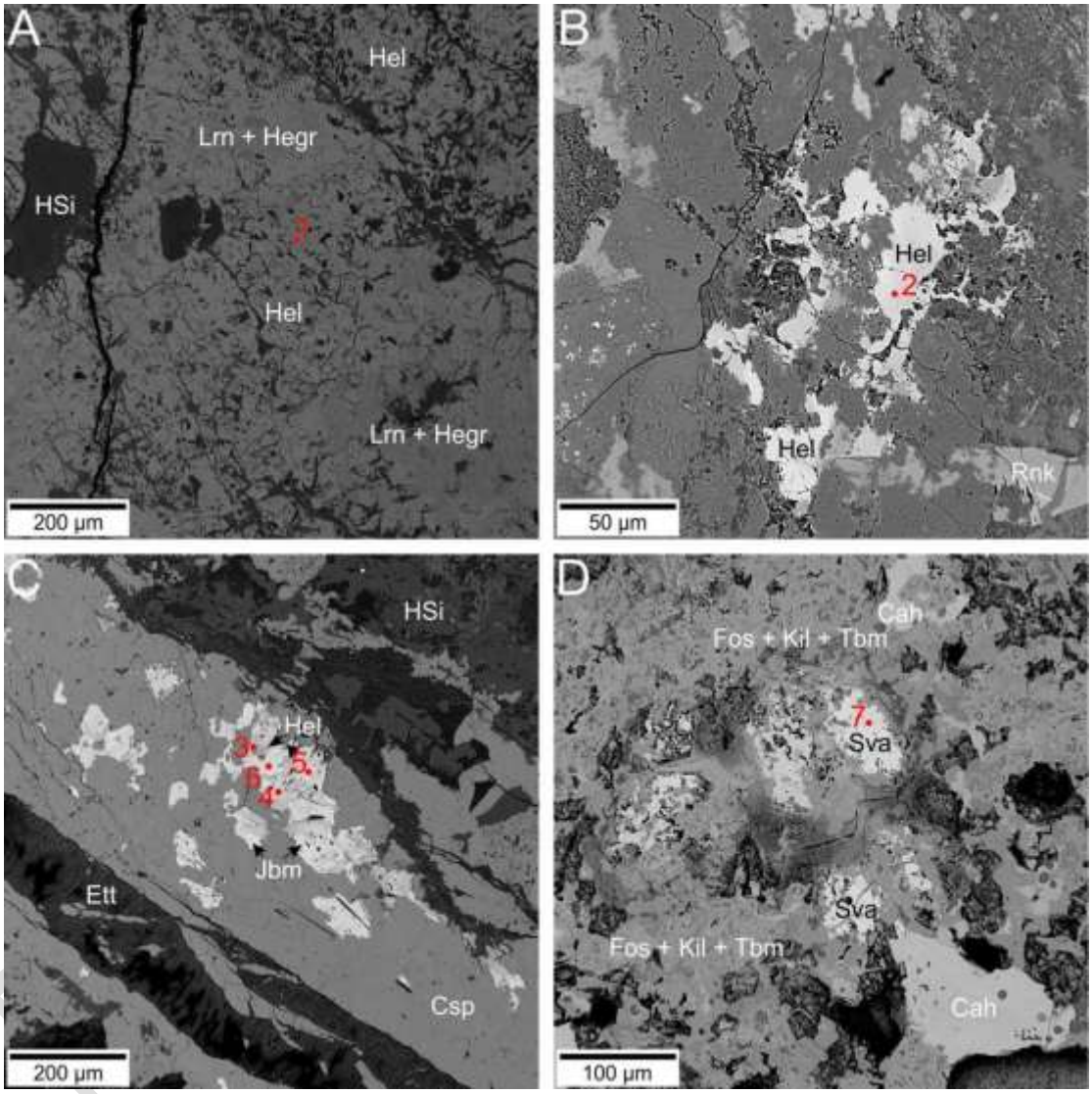

Fig. 4. BSE image of As-bearing minerals from different zones of xenolith no. 11. The red dots indicate the points of analysis in Table 1.

Mineral abbreviations: Csp - cuspidine, Cah - cahnite, Ett – ettringite, Fos - foshagite, Hel - hydroxylellestadite, Hegr – hydroxyledgrewite, HSi - unidentified hydrosilicates, Jbm - johnbaumite, Kil - killilaite, Lrn - larnite, Rnk – rankinite, Sva – svabite, Tbm – tobermorite

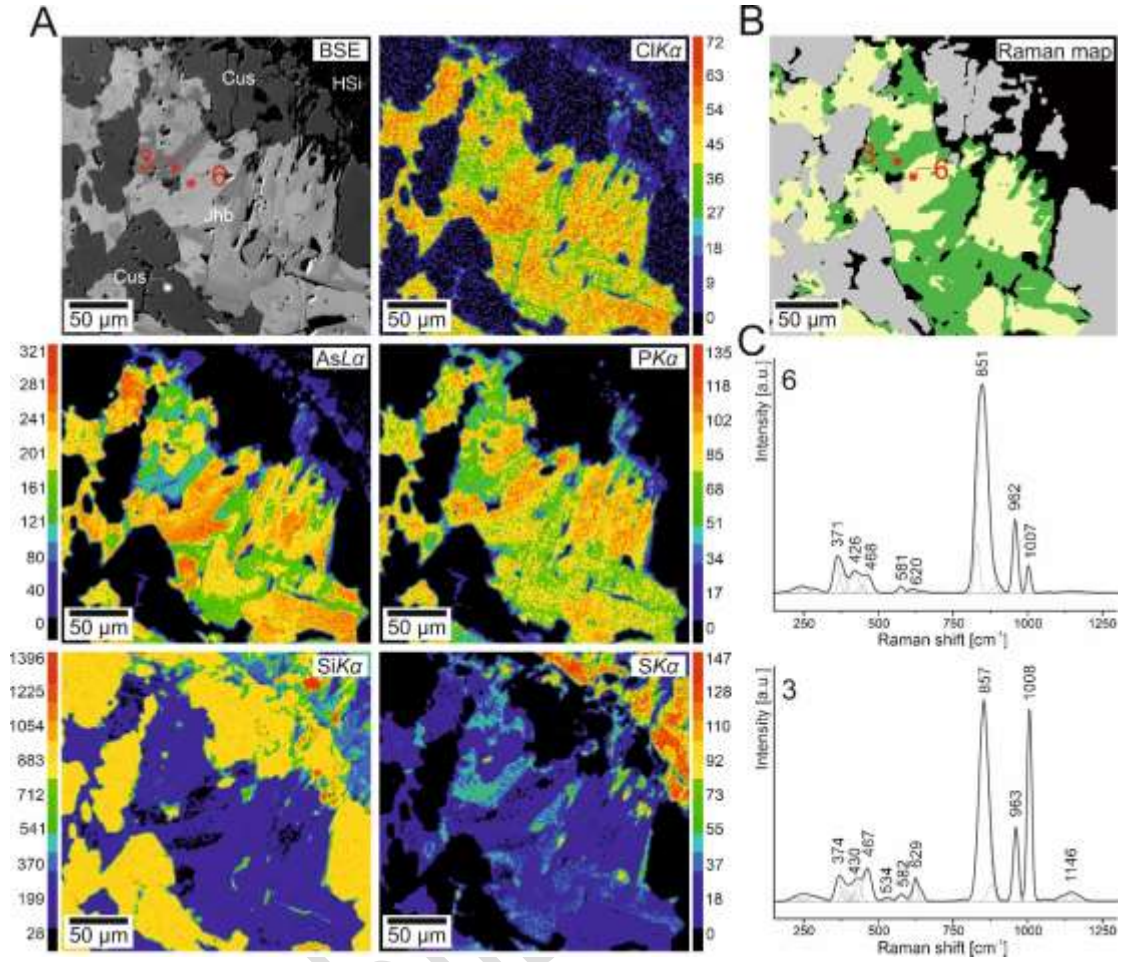

Fig. 5. A: BSE image and chemical mapping of the hydroxylellestadite-johnbaumite aggregate in the cuspidine vein based on an EMPA results. B: K-means cluster analysis of the hydroxylellestadite-johnbaumite aggregate shown in Fig. 5A; C: Raman spectra of hydroxylellestadite (3) and johnbaumite (6) from the cuspidine veins marked in the BSE image in Fig. 5A. The numbers in the spectrum correspond to the chemical composition in Table 1, points of analyses 6 and 3, respectively. Abbreviations: Csp - cuspidine, Hel - hydroxylellestadite, Jbm - johnbaumite, HSi - unidentified hydrosilicates.

The Raman study of the arsenic substitutions at the *T* site in the structure of the apatite supergroup minerals and their synthetic equivalents is an important

problem commonly discussed in the literature (Frost et al., 2007; Banasik et al. 2012; Gianfagna et al. 2014; Giera et al., 2016; Song et al., 2018; Lempart et al., 2019). The minerals found in the xenolith no. 11 allow following the changes through the application of Raman spectroscopy and the mutual correlation between the SiO_4/SO_4-AsO_4 ratio of these minerals (Fig. 6).

As a result, a closer look at the spectra collected from the samples analyzed revealed the most intense bands associated with symmetric stretching vibrations of SO_4 ν_1 (1006 cm^{-1}) and SiO_4 ν_1 (856 cm^{-1}), which are characterized by the ellestadite group minerals (Środek et al., 2018). The band at ca. 860 cm^{-1} is additionally interpreted as symmetric stretching vibrations of AsO_4 ν_1 when As is present at the *T* site (Gianfagna et al., 2014), while the band at ca. 961 cm^{-1} originates from symmetric stretching vibrations of the PO_4 ν_1 as in As-free members (Antonakos et al., 2007; Giera et al., 2016). However, this band can also be related to the asymmetric stretching vibrations of AsO_4 ν_3 in As-bearing phases (Song et al., 2018). A broad and low-intensity band around 1141 cm^{-1} corresponds to asymmetric stretching vibrations of SiO_4, SO_4, and PO_4 ν_3 (Antonakos et al., 2007; Comodi et al., 2016; Środek et al., 2018). The low-lying bands correspond to the deformational ν_4 vibrations of the SO_4 group (630 cm^{-1}), SiO_4 group (538 cm^{-1}), and PO_4 group (581 cm^{-1}) (Antonakos et al., 2007; Środek et al., 2018). In the range of 500 - 400 cm^{-1} low-intensity bands appear related to ν_2 vibrations of PO_4, SO_4 groups, and ν_4 vibrations of AsO_4 groups (Gianfagna et al., 2014; Banno et al., 2016, Środek et al., 2018). The maximum at 467 cm^{-1} is most probably related to ν_2 vibrations of SO_4 groups (Banno et al., 2016, Avdontceva et al., 2021), and the band at 426 cm^{-1} to ν_4 vibrations of AsO_4 groups (Gianfagna et al., 2014). The bands at 368 and 325 cm^{-1} are due to ν_2 vibrations of AsO_4 (Frost et al., 2007) and SiO_4 (Onac et al., 2006), respectively.

The Raman spectra of the minerals of the hydroxylellestadite- johnbaumite-svabite series reveal a gradual change in band intensity corresponding to the vibrations of anions occupying the *T* site. As a result, we found a correlation between the decrease in intensity of the SO_4-related bands and the simultaneous increase in arsenic content in the mineral composition. It is worth noting that the intensity of the band at 860 cm^{-1} does not decrease with decreasing silica content due to the overlapping nature of the symmetric stretching vibrations of SiO_4 and AsO_4. However, changes in the shape of the band indicated a structural deformation, confirming the Si↔As substitution.

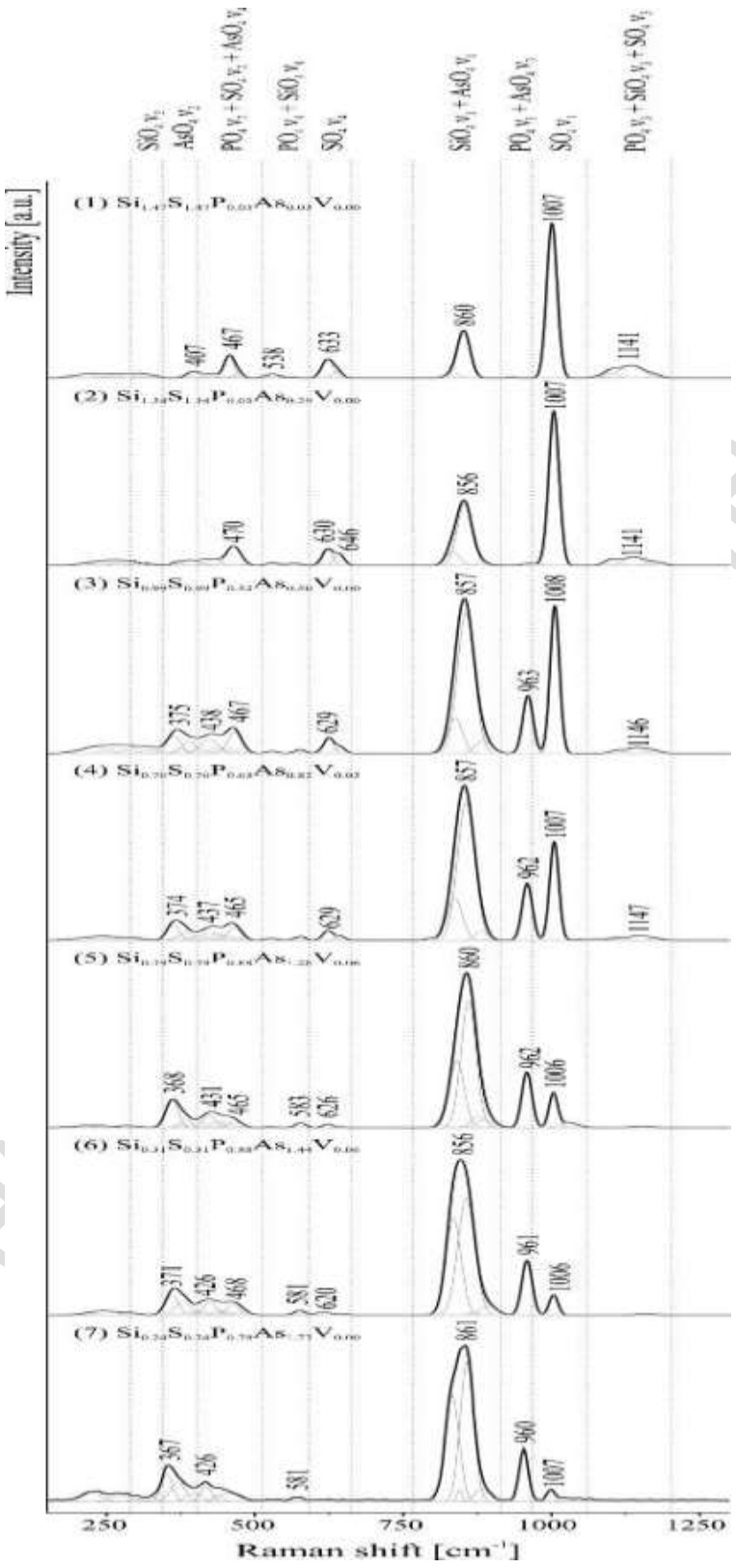

Fig. 6. Raman spectra of the hydroxylellestadite- johnbaumite-svabite mineral series from xenolith no. 11, Upper Chegem Caldera.

As- and B-bearing minerals associated with the apatite supergroup minerals

In this work we have identified several B- and/or As-bearing minerals in addition to the apatite supergroup minerals, such as cahnite, datolite, and the low-temperature bultfonteinite, $Ca_2(HSiO_4)F{\cdot}H_2O$. The highest B and As contents of borate and arsenate minerals were detected in the outer, altered zone adjacent to the ignimbrite (Fig. 1B). The core and middle zones of the xenolith contain much less B- and As-bearing minerals.

Cahnite

Cahnite was found in the outer altered zone (III) of the xenolith composed mainly of minerals of thaumasite-ettringite series, fluorite, tobermorite, calcite, Ca-Al hydrosilicates, bultfonteinite, and less common cuspidine, perovskite, lakargiite, and svabite. It forms irregular crystals up to 200 μm across (Fig. 4D, Fig. 7A, B). The empirical formula of cahnite from the Upper Chegem Caldera is $Ca_{2.00}B_{1.00}(As_{0.82}S_{0.06}Si_{0.06}P_{0.04}V_{0.02})_{\Sigma 1.00}O_4[(OH)_{3.95}F_{0.05}]_{\Sigma 4.00}$ (Table 2), and its composition is close to the ideal formula, $Ca_2B(AsO_4)(OH)_4$ and to those previously reported (Palache and Bauer, 1927; Shiraga et al., 2002). Some minor differences are reflected in insignificant impurities of S, Si, P, and V substituting As at the As-O tetrahedron and negligible presence of F substituting hydroxyl groups.

Table 2. Chemical composition of cahnite, cuspidine and hydroxyledgrewite from xenolith no. 11.

	cahnite mean 6			cuspidine mean 7			hydroxyledgrewite mean 8		
	wt%	range	s.d.	wt%	range	s.d.	wt%	range	s.d.
SO_3	1.64	0.60-1.90	0.77	n.d.	-	-	n.d.	-	-
P_2O_5	0.93	0.70-1.60	0.52	n.d.	-	-	n.d.	-	-
V_2O_5	0.52	0.00-2.04	0.98	n.d.	-	-	n.d.	-	-
SiO_2	1.33	1.04-3.92	1.36	32.60	32.27-33.33	0.31	31.01	30.62-33.76	1.01
As_2O_5	32.44	29.39-34.13	2.70	n.d.	-	-	n.d.	-	-
B_2O_3*	12.05	-	-	n.d.	-	-	n.d.	-	-
CaO	38.63	38.48-39.14	0.33	60.82	59.89-61.00	0.43	65.10	62.47-66.14	1.22
Cl	n.d.	-	-	n.d.	-	-	0.05	0.03-0.06	0.01
F	0.32	0.15-0.44	0.13	10.33	10.16-11.77	0.18	1.18	0.39-1.37	0.32
H_2O*	12.27			n.d.	-	-	1.76		
-O=F+Cl	0.13			4.35			0.51		
	100.00			99.41			98.58		
	Calculated on 4 cations			Calculated on 6 cations			Calculated on 13 cations		
S	0.06			-			-		
P	0.04			-			-		
V	0.02			-			-		
Si	0.06			2.00			4.00		
As	0.82			-			-		
B	1.00			-			-		
Ca	2.00			4.00			9.00		
Cl	-			-			0.01		
F	0.05			2.00			0.48		
OH	3.95			-			1.51		

Note: * - calculated on the basis of charge balance

To confirm the presence of boron and determine the area of its distribution in the grains the ToF-SIMS maps were obtained on the selected grain of cahnite. This analysis has confirmed the presence of boron; two peaks at m/z = 11 Da and m/z = 10

Da were assigned to ^{10}B and ^{11}B isotopes (not shown). Fig. 7 shows the distribution maps of $^{11}B^{+}$, Ca^{+}, and Mg^{+} reconstructed from the mass spectra resulting from the Fast Imaging Mode of the spectrometer operation. The ion distributions vary, and mineral phase boundaries are clearly visible. Boron has a homogeneous distribution in the area of the grains studied.

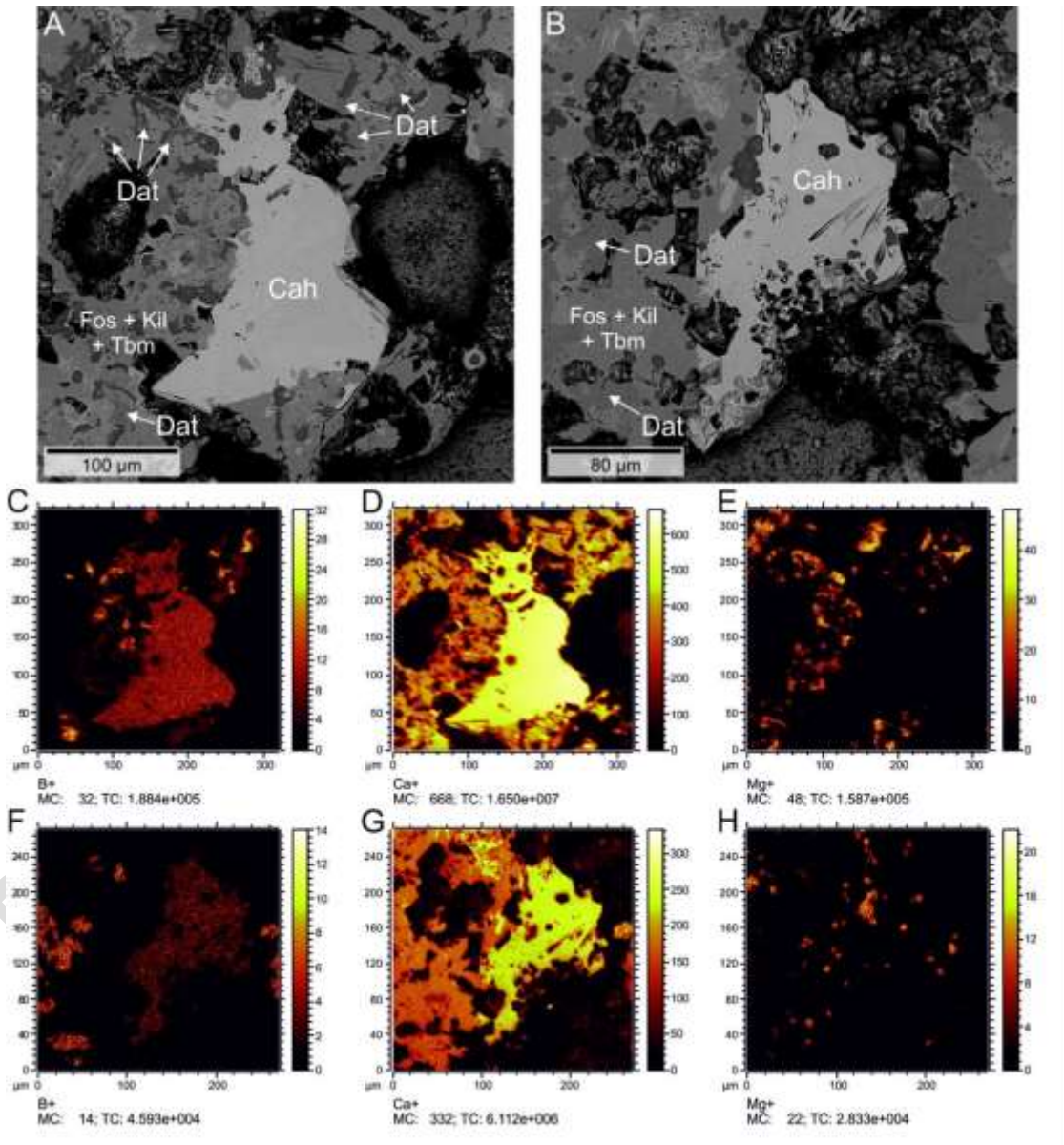

Fig. 7. A, B - BSE image of cahnite with datolite relic; C, D, E - T_OF-SIMS B, Ca and Mg images of cahnite grain and associated minerals in Fig. 7A; F, G, H - ToF-SIMS B, Ca and Mg images of cahnite grain and associated minerals in Fig. 7B.

Mineral abbreviations: Cah - cahnite, Dat – datolite, Fos - foshagite, Kil - killilaite, Tbm – tobermorite.

The Raman and IR spectra obtained are in agreement with previously published data (Ross, 1972; Shiraga et al., 2002). The main bands in the Raman and IR spectrum of cahnite (Fig. 8) are related to vibrations of borate and arsenate groups. The Raman spectrum of cahnite is mainly determined by the one intense band centred at 844 cm^{-1}, which is assigned to the the AsO_4 ν_1 group vibrations and other weaker ones originating from ν_3 (791 cm^{-1}), ν_2 (280 cm^{-1}) and ν_4 (443 cm^{-1}) (Ross, 1972). Arsenium in tetrahedral coordination was confirmed in the IR spectrum by the bands associated with the AsO_4^{3-} ν_1 and ν_3 vibrations observed in the 750-900 cm^{-1} region (Baykal & Evren, 2006).

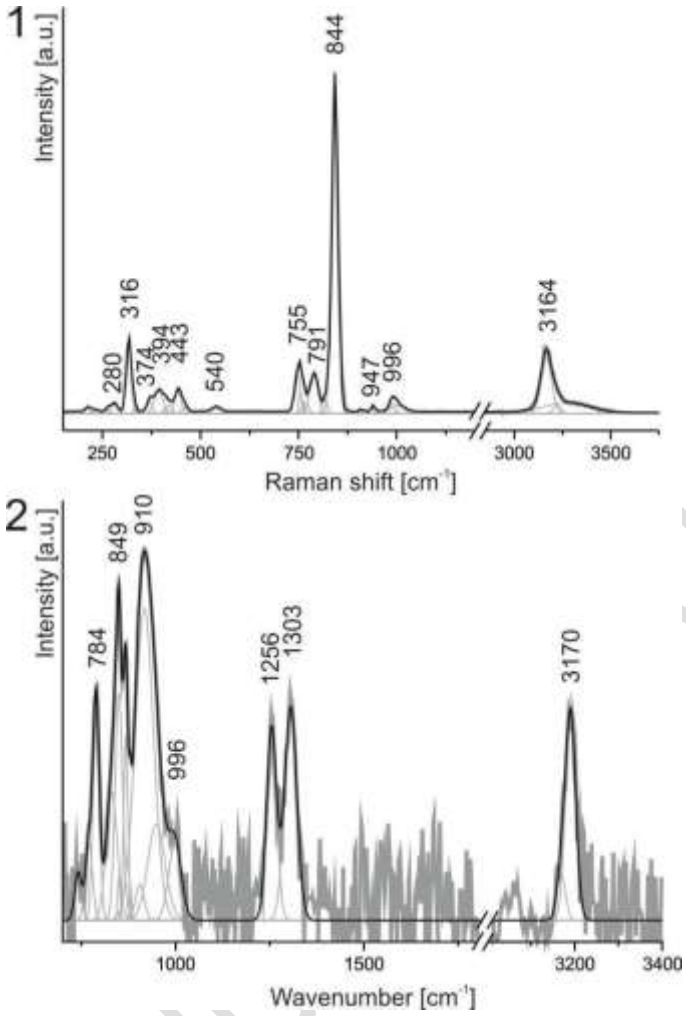

Fig. 8. The Raman (1) and infra-red (2) spectra of cahnite obtained *in situ* in the sample from the Upper Chegem Caldera xenolith.

Confirming the presence of boron in the structure of cahnite and its structural coordination (tetrahedral, triangular, diboron, etc.) and assigning the vibration type to the B-O bond is challenging. Assuming the structural correctness of cahnite as reported by Prewitt and Buerger (1961), boron tetrahedrally coordinated by hydroxyl groups at each apex should exhibit in the Raman spectrum both symmetric and asymmetric stretching vibrations of $B(OH)_4^-$ ν_1 (755 cm^{-1}), and ν_3 (947 cm^{-1}) as well as deformational bending modes ν_2 (374 / 394 cm^{-1}), and ν_4 (540 cm^{-1}) (Edwards et al., 1955; Ross, 1972). There are only a few papers describing boron-phase minerals,

making the interpretation and assignment of Raman bands problematic. Therefore, we have decided to correlate Raman spectroscopy data with infrared data to better understand the possible presence of boron in the structure of cahnite.

The interpretation of the IR spectrum proved to be somewhat more complicated due to the limited literature on boron-related phases, indicating that boron can also occur in non-protonated tetrahedral coordination, as evidenced by the symmetric stretching vibrations of the [BO_4] group correlated to the band at 996 cm^{-1} (Balachander et al., 2013). In addition, asymmetric stretching vibrations of hydroxylated tetrahedral boron coordination can be assigned to the band at 933 cm^{-1} (ν_3 $B(OH)_4$) (Ross, 1972). The infrared spectrum of cahnite also reveals the possible occurrence of boron in a triangular, spatially planar configuration, which contributes to the activation of two very intense bands at 1256 and 1303 cm^{-1} originating from the asymmetric and symmetric stretching vibrations of B-O bonds in the [BO_3] units, respectively (Jun et al., 1994; Balachander et al., 2013; Shiraga et al., 2002).

It is important to note that a polyborate anion, consisting of a BO_3 planar triangle and protonated or deprotonated BO_4 tetrahedra, may potentially exist.. However, the vibrations within the BO_3 unit are Raman inactive. This theory could be confirmed by repeating single-crystal structural refinement, although this issue is not the subject of this article and will be developed in a separate article.

Finally, the Raman and infrared bands observed in-between 3000-3500 cm^{-1} confirm the hypothesis about $B(OH)_4^-$ units. The Raman spectrum has shown a sharp, intense band at 3164 cm^{-1} and another low, intense band around 3400 cm^{-1}. The band at 3164 cm^{-1} in the Raman spectrum corresponds to a hydroxyl-related band reported by Shiraga et al. (2002) for the IR spectrum of cahnite. A similar value was observed in our IR spectrum (3170 cm^{-1}). According to Prewitt and Buerger (1961), this band is

probably arranged in the hydrogen bonds (O_d-O_a=2.795Å), confirming the hypothesis of the presence of $B(OH)_4^-$. Another weak band around 3400 cm^{-1} is related to the sorbed hydroxyl groups or results from another internal interaction due to specific structural arrangements such as polyborate and arsenic units.

Datolite

The ToF-SIMS results revealed another boron-rich mineral in the mass of secondary minerals around cahnite, which, according to the EDS analyses, is a borosilicate with a Ca:Si ratio of 1:1. The TOF-SIMS distribution maps of boron indicate regions with significantly higher counts (greater intensity) compared to the cahnite phase, as demonstrated in Figures 7C and 7D. The obtained Raman spectrum (Fig. 9) allowed this phase to be identified as datolite, $CaBSiO_4(OH)$. It forms small grains intergrown with low-temperature Ca-hydrosilicates (Fig. 7A, B).

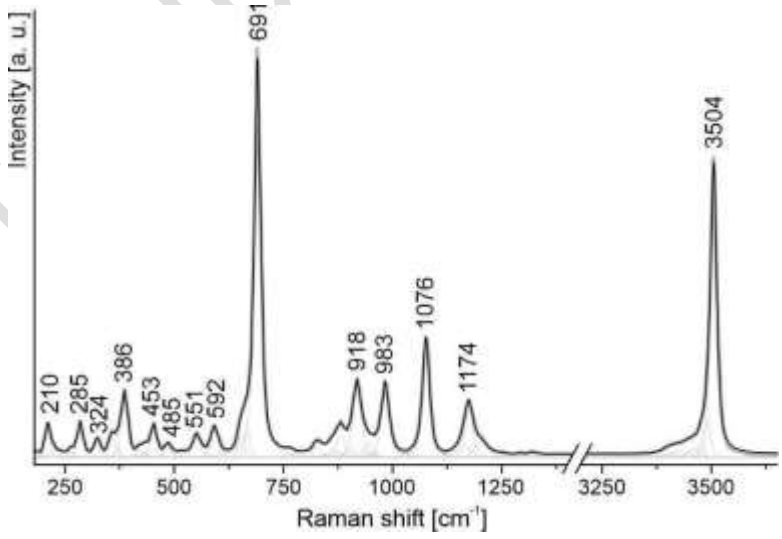

Fig. 9. Raman spectrum of datolite from xenolith no. 11.

The Raman spectrum of datolite from the Upper Chegem Caldera is almost identical to spectra for this mineral obtained from other localities (Frost et al., 2013; Goryainov et al., 2014; Bailey et al., 2019; Yoshida et al., 2021). The main high intensity bands in the 600-1200 cm^{-1} range are associated with "breathing" modes of four- and eight-membered rings (Goryainov et al., 2014). Bands related to the symmetric and asymmetric B-O vibrations are assigned to bands at 918 and 983 cm^{-1}, respectively (Frost et al., 2013; Bailey et al., 2019). The bands associated with the symmetric and asymmetric modes of Si-O assigned to bands at 1076 and 1174 cm^{-1} (Frost et al., 2013; Bailey et al., 2019). The 691 cm^{-1} band has been attributed to the deformational vibrations of tetrahedral B-O bonds (Frost et al., 2013; Bailey et al., 2019). The low intensity bands below 600 cm^{-1} are associated with the external modes of tetrahedra, rings, and chains of silicate minerals (Goryainov et al., 2014). The band at 3504 cm^{-1} is related to stretching vibrations of OH groups in datolite (Frost et al., 2013; Bailey et al., 2019).

Discussion

The members of the apatite supergroup minerals discovered in xenolith no. 11 within the Upper Chegem Caldera provide a unique opportunity to study the effect of chemical composition in the Raman spectra, in particular, variations in the SiO_4/SO_4-AsO_4 ratio at the *T* site in the structure. Our study shows that even a small change in the occupancy of the tetragonal sites affects the shape of the Raman spectrum. Thus, it can be used as a preliminary non-destructive method to distinguish group members within the apatite supergroup. However, according to the authors, a more precise assignment to a specific mineral species is currently not possible because of a lack of

spectroscopic studies focusing on the effect of the occupancy of the *X* site in the structural channel on the shape of the spectrum, apart from a band appearing at 3568 cm^{-1} associated with the OH group vibrations. To be certain, further studies are needed on apatite supergroup minerals with equal occupancies within the *T* site but with different substitutions in the structural channels. At the same time, the analyses carried out have shown the occurrence of a solid-solution system between hydroxylellestadite, svabit, and johnbaumite, which has not been previously described.

In view of the wide chemical diversity of the studied apatite supergroup minerals, it is necessary to consider the genesis of the mineral association presented in this paper. The first important issue is the source of arsenic and boron contained in the mineral paragenesis of calcium-silicate xenoliths from the Upper Chegem caldera. The research presented shows that the B and As contents in the minerals of xenolith no. 11 change with distance from the xenolith-ignimbrite contact. The higher contents of these elements in the minerals were confirmed in the outermost, altered zone (III) adjacent to the ignimbrite. The central zone (I) of the xenolith is characterised by lower boron and arsenic contents in minerals (Fig. 4A, B; Table 1.1-2).

Investigations of the mineral and isotopic composition of the ignimbrites from the Upper Chegem caldera and surrounding rocks show no evidence of pre-caldera volcanism (Gazis, 1995). They ruled out the existence of extensive post-caldera hydrothermal alteration (Gazis, 1995). It shows that boron and arsenic could either have been present in the protolith rocks prior to pyrometamorphic processes or were introduced into the system with the intrusion of rhyodacite lavaBoron is a readily leached element (Schmitt et al., 2002) and is, therefore, generally removed from rocks during metamorphic processes (Palmer & Swihart, 1996). Considering this, and also

the presence of boron in the outer zone of the xenolith, the presence of this element in the calcium protolith seems unlikely. On the other hand, ignimbrites are a proven carrier of boron and are commonly cited as a potential source of B for borate deposits (Alonso et al., 1990; Floyd et al., 1998). Woodford et al. (2001) also demonstrated that the formation of boron-rich skarn minerals is related to the magmatic source of this element. In addition to boron, volcanic rocks are common sources of arsenic (Murray et al., 2023). In particular, rocks containing a significant amount of silica, such as rhyolites, dacites, and ignimbrites, are characterized by a high arsenic content (Mazzuoli et al., 2014; Murray et al., 2023). It is worth to notice, that arsenic is a volatile element that is a typical component of volcanic gases (Pekov et al., 2018). Hence, it is possible to incorporate this element into metamorphic rocks with fluids associated with magma injection.

Therefore, it is reasonable to assume that ignimbrite was the source of boron and arsenic for the formed minerals within the Upper Chegem caldera xenoliths.

Another critical issue is the order of crystallization of the apatite supergroup minerals. Given the occurrence of only one metamorphic episode associated with the rhyodacite intrusion, it should be assumed that all the minerals belonging to the apatite supergroup crystallized simultaneously. This theory is also supported by the co-occurrence of hydroxylellstadite and johnbaumite within the cuspidine veins. These crystallize as aggregates composed of independent individuals with different chemical compositions. If johnbaumite was related to the alteration of hydroxylellstadite, crystals with zoning associated with different levels of arsenic in the structure would be formed. However, we are presented with mostly homogeneous crystals in terms of chemical composition. It is also interesting to note the presence of cahnite in the described mineral association. Shiraga et al., (2002) suggest that cahnite

is a secondary mineral formed by hydrothermal alteration of johnbaumite. Given the co-occurrence of cahnite and svabite in the xenolith from the Upper Chegem Caldera, it is necessary to exclude the possibility that this mineral formed as a secondary phase that developed after the apatite supergroup minerals in this case. Helvaci (2015) reports that cahnite forms as a secondary mineral after the low-temperature mineral - colemanite, due to diagenetic alteration. He shows that other B-bearing minerals can also be precursors of cahnite. Given the occurrence of datolite relics in the vicinity of cahnite suggests that datolite was the parent mineral for cahnite. The explanation for the genesis of datolite is more problematic, as it can occur in a wide range of geological environments (Goryainov et al., 2014).

Acknowledgements

We want to thank Dr Viktor Gazeev for his help in collecting the rock samples. We thank Prof. Evgeny Galuskin and Prof. Irina Galuskin for their valuable comments and help during the preparation of the manuscript.

Competing Interests: The author(s) declare none.

References

Alonso, R.N., Viramonte, J.G. (1990) Borate deposits in the Andes. Pp. 721-732 in: *Stratabound Ore Deposits in the Andes* (L. Fontboté, G.C. Amstutz, M. Cardozo, E. Cedillo, J. Frutos, editors), Springer-Verlag, Berlin, Heidelberg.

Antonakos A., Liarokapis E. and Leventouri T. (2007) Micro-Raman and FTIR studies of synthetic and natural apatites. *Biomaterials*, **28**, 3043-3054.

Avdontceva M., Zlototarev A., Krivovichev S., Krzhizhanovskaya M., Sokol E., Kokh S., Bocharov V., Rassomakhin M. and Zlototarev A. (2021) Fluorellestadite from burned coal dumps: crystal structure refinement, vibrational spectroscopy data and thermal behavior. *Mineralogy and Petrology*, **115**, 1-11.

Bailey D., Lupulescu M., Darling R., Singer J. and Chamberlain S. (2019) A review of boron-bearing minerals (excluding tourmaline) in the Adirondack region of New York State. *Minerals*, **9**, art. no. 644.

Balachander L., Ramadevudu G., Shareefuddin M., Sayanna R. and Venudhar Y. (2013) IR analysis of borate glasses containing three alkali oxides. *ScienceAsia*, **39**, 278-283.

Banasik K., Galuskin E., Armbruster T., Lazic B., Galuskina I. and Gazeev V. (2012) Apatite supergroup minerals of the solid solution $Ca_5[(PO_4)_{3-x}(AsO_4)_x]_{\Sigma 3-2y}[(SO_4)_y(SiO_4)_y]_{\Sigma 2y}(OH, F, Cl)$, x = 0-3, y = 0-1.5, from high temperature skarn of the Upper Chegem caldera, Northern Caucasus, Russia. Pp. 298 in: *Book of abstracts*. European Mineralogical Conference, Frankfurt Meeting, September 2012.

Banno Y., Miyawaki R., Momma K. and Bunno M. (2016) A CO_3-bearing member of the hydroxylapatite-hydroxylellestadite series from Tadano, Fukushima Prefecture, Japan: CO_3-SO_4 substitution in the apatite-ellestadite series. *Mineralogical Magazine*, **80**, 363-370.

Baykal A. and Evren A. (2006) Hydrothermal and microwave-assisted synthesis of boroarsenate, $BAsO_4$. *Turkish Journal of Chemistry*, **30**, 723-730.

Bersani D., Andò S., Scrocco L., Gentile P., Salvioli-Mariani E., Fornasini L. and Lottici P. (2019) Composition of amphiboles in the tremolite-ferro-actinolite series by Raman spectroscopy. *Minerals*, **9**, 491.

Biagioni C. and Pasero M. (2013) The crystal structure of johnbaumite, $Ca_5(AsO_4)_3OH$, the arsenate analogue of hydroxylapatite. *American Mineralogist*, **98**, 1590-1584.

Biagioni C., Bosi F., Hålenius U. and Pasero M. (2016) The crystal structure of svabite $Ca_5(AsO_4)_3F$, an arsenate member of the apatite supergroup. *American Mineralogist*, **101**, 1750-1755.

Bogatikov O., Gurbanov A., Kovalenko V., Koronovsky N., Lipman P. and Tsvetkov A. (1992) The Upper Chegem caldera complex in Northern Caucasus. *International Geology Review*, **34**, 131-147.

Comodi P., Liu Y., Stoppa F. and Woolley A. (2016) A multi-method analysis of Si-,S- and REE-rich apatite from a new find of kalsilite-bearing leucitite (Abruzzi, Italy). *Mineralogical Magazine*, **63**, 661-672.

Edwards J., Morrison G., Ross V. and Schultz J. (1955) The structure of the aqueous borate ion. *Journal of the American Chemical Society*, **77**, 266-268.

Fearn S. (2015) An introduction to time-of-flight Secondary Ion Mass Spectrometry (TOF-SIMS) and its application to materials science. Morgan & Claypool, London.

Floyd P., Helvaci C. and Mittwede S. (1998) Geochemical discrimination of volcanic rocks associated with borate deposits; an exploration tool? *Journal of Geochemical Exploration*, **60**, 85 - 205.

Frost R., Bouzaid J. and Palmer S. (2007) The structure of mimetite, arsenian pyromorphite and hedyphane - A Raman spectroscopic study. *Polyhedron*, **26**, 2964-2970.

Frost R., Xi Y., Scholz R., Lima R., Horta L. and Lopez A. (2013) Thermal analysis and vibrational spectroscopic characterization of the boro silicate mineral datolite –

$CaBSiO_4(OH)$. *Spectrochimica Acta Part A: Molecular and Biomolecular spectroscopy,* **115**, 376-381.

Galuskin E., Galuskina I., Kusz J., Gfeller F., Armbruster T., Bailau R., Dulski M., Gazeev V., Pertsev N., Zadov A. and Dzierżanowski P. (2015) Mayenite supergroup, part II: Chlorkyuygenite from Upper Chegem, Northern Caucasus, Kabardino-Balkaria, Russia, a new microporous mineral with "zeolitic" H_2O. *European Journal of Mineralogy*, **26**, 113-122.

Galuskina I., Krüger B., Galuskin E., Armbruster T., Gazeev V., Włodyka R., Dulski M. and Dzierżanowski P. (2015) Fluorchegemite, $Ca_7(SiO_4)_3F_2$, a new mineral from the edgrewite-bearing endoskarn zone of an altered xenolith in ignimbrites from Upper Chegem caldera, Northern Caucasus, Kabardino-Balkaria, Russia: occurrence, crystal structure, and new data on the mineral assemblages. *The Canadian Mineralogist*, **53**, 325-344.

Galuskina I., Galuskin E., Środek D. and Gazeev V. (2018) Potentially new Cl-bearing minerals from xenolith of the Upper Chegem Caldera, Northern Caucasus, Russia. Pp. 525 in: *Book of Abstracts of the XII Meeting of the International Mineralogical Association.* Geological Society of Australia, Melbourne Meeting, August 2018.

Gazis C. (1995) An isotopic study of the fluid flow and thermal history of the 2.8 Ma Chegem ash-flow caldera and related intrusive rocks (Caucasus Mountains, Russia). PhD dissertation, California Institute of Technology, USA.

Gianfagna A., Mazziotti-Tagliani S., Croce A., Allegrina M. and Rinuado C. (2014) As-rich apatite from Mt. Calvario: characterization by micro-Raman spectroscopy. *The Canadian Mineralogist*, **52**, 799-808.

Giera A., Manecki M., Bajda T., Rakovan J., Kwaśniak-Kominek M. and Marchlewski T. (2016) Arsenate substitution in lead hydroxyl apatites: A Raman spectroscopic study. *Spectrochimica Acta Part A: Molecular and Biomolecular Spectroscopy*, **152**, 370-377.

Goryainov S., Krylov A., Vtyurin A. and Pan Y. (2014) Raman study of datolite $CaBSiO_4(OH)$ at simultaneouslty high pressure and high temperature. *Journal of Raman spectroscopy*, **46**, 177-181.

Hagenhoff B. (2000) High resolution surface analysis by TOF-SIMS. *Microchimica Acta*, **132**, 259-271.

Helvaci C. (2015) Review of the occurrence of two new minerals in the Emet borate deposit, Turkey: Emetite, $Ca_7Na_3K(SO_4)_9$, and fontarnauite, $Na_2Sr(SO_4)[B_5O_8(OH)](H_2O)_2$. *Bulletin of the Mineral Research and Exploration*, **151**, 269-283.

Jun L., Shuping X., Shiyang G. (1994) FT-IR and Raman spectroscopic study of hydrated borates. *Spectrochimica Acta*, **51A**, 519-532.

Lazic B., Armbruster T., Galuskina I., Zieliński G., Dzierżanowski P. and Galuskin E. (2012) B- and As-bearing galuskinite and B-analog of galuskinite from Upper Chegem caldera, Northern Caucasus, Russia. Pp. 298 in: *Book of abstracts*. European Mineralogical Conference, Frankfurt Meeting, September 2012.

Leissner L., Schlüter J., Horn I. and Mihailova B. (2015) Exploring the potential of Raman spectroscopy for crystallochemical analyses of complex hydrous silicates: I. Amphiboles. *American Mineralogist*, **10**, 2682-2694.

Lempart M., Manecki M., Kwaśniak-Kominek M., Matusik J. and Bajda T. (2019) Accommodation of the carbonate ion in lead hydroxyl arsenate (hydroxylmimetite) $Pb_5(AsO_4)_3OH$. *Polyhedron*, **161**, 330-337.

Mazzuoli M., Armiento G., Crovato C., Nardi E. and Proposito M. (2014) Influence of water-rock interaction and of uprising deep fluids on the arsenic content in the groundwater of Viterbo area. Pp. 114 in: Flowpath 2014 – National Meeting on Hydrogeology, Viterbo Meeting, June 2014.

Murray J., Guzmán S., Tapia J. and Nordstorm D. (2023) Silicic volcanic rocks, a main regional source of geogenic arsenic in waters: Insights from the Altiplano-Puna plateau, Central Andes. *Chemical Geology*, **629**, 121473.

Onac B., Effenberger H., Ettinger K. and Panzaru C. (2006) Hydroxylellestadite from Cioclovina Cave (Romania): Microanalytical, structural, and vibrational spectroscopy data. *American Mineralogist*, **91**, 1927-1931.

Palache C. and Bauer L. (1927) Cahnite, a new boroarsenate of calcium from Franklyn, New Jersey. *American Mineralogist*, **12**, 149 - 153.

Palmer M. and Swihart G. (1996) Boron isotope geochemistry: an overview. Pp. 709-744 in: *Boron: Mineralogy, Petrology and Geochemistry* (E.S. Grew, L.M. Anovitz, editors) De Gruyter, Berlin, Boston.

Pasero M., Kampf A., Ferraris C., Pekov I., Rakovan J. and White T. (2010) Nomenclature of the apatite supergroup minerals. *European Journal of Mineralogy*, **22**, 163-179.

Pekov I., Koshlyakova N., Zubkova N., Lykova I., Britvin S., Yapaskurt V., Agakhanov A., Shchipalkina N., Turchkova A., Sidorov E. (2018) Fumarolic arsenates - a special type of arsenic mineralization. *European Journal of Mineralogy*, 30, 305-322.

Prewitt C. and Buerger M. (1961) The crystal structure of cahnite $Ca_2BAsO_4(OH)_4$. *American Mineralogist*, **46**, 1077-1085.

Ptáček P. (2016) Substitutents and dopants in the structure of apatite. In: *Apatites and their synthetic analogues* (Ptáček P. editor). IntechOpen, London.

Ross S. (1972) The vibrational spectra of some minerals containing tetrahedrally coordinated boron. *Spectrochimica Acta*, **28A**, 1555-1561.

Schmitt A., Kasemann S., Meixner A. and Rhede D. (2002) Boron in central Andean ignimbrites: implications for crustal boron cycles in an active continental margin. *Chemical Geology*, **183**, 333-347.

Shiraga K., Kusachi I., Kobayashi S. and Takechi Y. (2002) Cahnite from Fuka, Okayama Prefecture, Japan. *Journal of Mineralogical and Petrological Sciences*, **97**, 70-73.

Siljeström S., Parenteau M., Jahnke L. and Cady S. (2017) A coparative TOF-SIMS and GC-MS analysis of phototrophic communities collected from an alkaline silica-depositing hot spring. *Organic Geochemistry*, **109**, 14-30.

Song H., Liu J. and Cheng H. (2018) Structural and spectroscopic study of arsenate and vanadate incorporation into apatite group: Implications for semi-quantitative estimation of As and V contents in apatite. *Spectrochimica Acta Part A: Molecular and Biomolecular Spectroscopy*, **188**, 488-494.

Środek D., Galuskina I., Galuskin E., Dulski M., Książek M., Kusz J. and Gazeev V. (2018) Chlorellestadite, $Ca_5(SiO_4)_{1.5}(SO_4)_{1.5}Cl$, a new ellestadite-group mineral from the Shadil-Khokh volcano, South Ossetia. *Mineralogy and Petrology*, **112**, 743-752.

Varlamov D., Ermolaeva V., Chukanov N., Jančev S., Vigasina M. and Plechov P. (2020) New data on epidote-supergroup minerals: unusual chemical compositions, typochemistry, and Raman spectroscopy. *Geology of Ore Deposits*, **61**, 827-842.

Watenphul A., Burgdorf M., Schlüter J., Horn I., Malcherek T. and Mihailova B. (2016) Exploring the potential of Raman spectroscopy for crystallochemical analyses of complex hydrous silicates: II. Tourmalines. *American Mineralogist*, **101**, 970-985.

Woodford D., Sisson V. and Leeman W. (2001) Boron metasomatism of the Alta stock contact aureole, Utah: Evidence from borates, mineral chemistry, and geochemistry. *American Mineralogist*, **86**, 513 -533.

Yoshida K., Niki S., Sawada H. and Oyanagi R. (2021) Discovery of datolite in a high-pressure marble from the Sanbagawa metamorphic belt: Indication of B-rich fluid activity. *Journal of Mineralogical and Petrological Sciences*, **116**, 1-8.

Zadov A., Pekov I., Zubkova N., Gazeev V., Chukanov N., Yapaskurt V., Kartasheov P., Galuskin E., Galuskina I., Pertsev N., Gurbanov A. and Pushcharovsky D. (2013) *Geology of Ore Deposits*, **55**, 541-548.